



Flash Ionization Signatures in the Type Ibn Supernova SN 2019uo

Anjasha Gangopadhyay^{1,2}, Kuntal Misra^{1,3}, Daichi Hiramatsu^{4,5}, Shan-Qin Wang⁶, Griffin Hosseinzadeh⁷, Xiaofeng Wang⁸, Stefano Valenti³, Jujia Zhang⁹, D. Andrew Howell^{4,5}, Iair Arcavi^{10,11}, G. C. Anupama¹², Jamison Burke^{4,5}, Raya Dastidar^{1,13}, Koichi Itagaki¹⁴, Brajesh Kumar¹², Brijesh Kumar¹, Long Li⁶, Curtis McCully^{4,5}, Jun Mo⁸, Shashi Bhushan Pandey¹, Craig Pellegrino^{4,5}, Hanna Sai⁸, D. K. Sahu¹², Pankaj Sanwal^{1,2}, Avinash Singh^{12,15}, Mridweeka Singh^{1,16}, Jicheng Zhang⁸, Tianmeng Zhang¹⁷, and Xinhan Zhang⁸

¹ Aryabhata Research Institute of observational scienceS, Manora Peak, Nainital, 263002, India; anjasha@aries.res.in, anjashagangopadhyay@gmail.com

² School of Studies in Physics and Astrophysics, Pandit Ravishankar Shukla University, Chattisgarh 492010, India

³ Department of Physics, University of California, 1 Shields Avenue, Davis, CA 95616-5270, USA

⁴ Las Cumbres Observatory, 6740 Cortona Drive Suite 102, Goleta, CA, 93117-5575, USA

⁵ Department of Physics, University of California, Santa Barbara, CA 93106-9530, USA

⁶ Guangxi Key Laboratory for Relativistic Astrophysics, School of Physical Science and Technology, Guangxi University, Nanning 530004, People's Republic of China

⁷ Center for Astrophysics | Harvard & Smithsonian, 60 Garden Street, Cambridge, MA 02138-1516, USA

⁸ Physics Department and Tsinghua Center for Astrophysics, Tsinghua University, People's Republic of China

⁹ Yunnan Astronomical Observatory of China, Chinese Academy of Sciences, Kunming, 650011, People's Republic of China

¹⁰ The School of Physics and Astronomy, Tel Aviv University, Tel Aviv 69978, Israel

¹¹ CIFAR Azrieli Global Scholars program, CIFAR, Toronto, Canada

¹² Indian Institute of Astrophysics, Koramangala 2nd Block, Bangalore 560034, India

¹³ Department of Physics & Astrophysics, University of Delhi, Delhi-110007, India

¹⁴ Itagaki Astronomical Observatory, Japan

¹⁵ Joint Astronomy Programme, Department of Physics, Indian Institute of Science, Bengaluru 560012, India

¹⁶ Korea Astronomy and Space Science Institute, 776 Daedeokdae-ro, Yuseong-gu, Daejeon 34055, Republic Of Korea

¹⁷ National Astronomical Observatory of China, Chinese Academy of Sciences, Beijing, 100012, People's Republic of China

Received 2019 October 25; revised 2019 December 3; accepted 2019 December 16; published 2020 February 4

Abstract

We present photometric and spectroscopic observations of the type Ibn supernova (SN) 2019uo, the second ever SN Ibn with flash ionization (He II, C III, N III) features in its early spectra. SN 2019uo displays a rapid post-peak luminosity decline of 0.1 mag day^{-1} similar to most of the SNe Ibn, but is fainter ($M_{\text{max}}^V = -18.30 \pm 0.24 \text{ mag}$) than a typical SN Ibn and shows a color evolution that places it between SNe Ib and the most extreme SNe Ibn. SN 2019uo shows P-cygni He I features in the early spectra which gradually evolve and become emission dominated post peak. It also shows faster evolution in line velocities as compared to most other members of the type Ibn subclass. The bolometric light curve is fairly well described by a $^{56}\text{Ni} + \text{circumstellar interaction model}$.

Unified Astronomy Thesaurus concepts: Core-collapse supernovae (304); Supernovae (1668); CCD photometry (208); Photometry (1234); Spectroscopy (1558); Astronomical techniques (1684)

1. Introduction

Supernovae (SNe) undergoing interaction with a circumstellar medium (CSM) provide a unique window in the evolutionary phases of stars. Interaction, in general, produces narrow emission lines—broader than H II regions but narrower than lines arising from the outer ejecta of the supernova (Hosseinzadeh et al. 2017). However, in some cases interaction happens below the photosphere without any observable narrow emission lines (e.g., Morozova et al. 2017; Andrews & Smith 2018). SNe IIn (Schlegel 1990) and SNe Ia-CSM display narrow H lines indicative of interaction with a H-rich CSM. Approximately 1% of core-collapse SNe (CCSNe) show little H and narrow He features ($\sim 2000 \text{ km s}^{-1}$). With the discovery of SN 2006jc, Pastorello et al. (2007) introduced this class as SNe Ibn, whose spectral features show interaction signatures between SN ejecta and a He-rich CSM. This is defined in analogy with SNe IIn, which show narrow H features (Schlegel 1990). SNe that are embedded in dense CSM may also show short-lived narrow high ionization emission lines (≤ 10 days) owing to the recombination of the CSM following the shock breakout flash. These features are known as “flash features” (e.g., Gal-Yam et al. 2014). Hosseinzadeh et al. (2017) analyzed a sample of SN Ibn light curves and

showed that unlike SNe IIn, SNe Ibn are rather uniform in their light-curve shape with rapid decay rates of $0.05\text{--}0.15 \text{ mag day}^{-1}$. SNe Ibn may have double-peaked light curves like SNe IIn, but they show a faster rise than SNe IIn (Hosseinzadeh et al. 2017). On the other hand, Pastorello et al. (2016) showed that the class is heterogeneous with many outliers: OGLE-2012-SN-006 (Pastorello et al. 2015d) has a very slow decline; LSQ13ccw (Pastorello et al. 2015b) is faint and fast-declining; SNe 2005la and 2011hw (Pastorello et al. 2015a) are transitional type IIn/Ibn events; SN 2010al (Pastorello et al. 2015a) is the earliest detected SN Ibn with a slow rise and decline. Karamahmetoglu et al. (2019) recently identified a rapid evolving SN 2018bcc. SNe Ibn have bluer continuum than other CCSNe. Some SNe Ibn show P-cygni He I emission, while others transition from narrow to intermediate-width He I emissions (Hosseinzadeh et al. 2017).

So far, only indirect progenitor constraints for SNe Ibn are available. Pastorello et al. (2007) suggest that Wolf–Rayet (WR) H-free atmospheres generate the He-rich CSM. The best studied case for unstable mass loss from a WR progenitor is SN 2006jc, for which an optical transient was detected at the SN location two years prior to explosion (Foley et al. 2007; Pastorello et al. 2007; Smith et al. 2008). Alternatively, CSM can be produced by stripping material from envelopes of

Table 1
Photometry of SN 2019uo

Date (yyyy-mm-dd)	JD (2458000+)	Phase ^a (day)	<i>U</i> (mag)	<i>B</i> (mag)	<i>g</i> (mag)	<i>V</i> (mag)	<i>r</i> (mag)	<i>i</i> (mag)	Telescope
2019 Jan 18	501.8	−6.8	...	17.865 ± 0.107	17.637 ± 0.097	17.927 ± 0.146	17.936 ± 0.139	...	LCO
2019 Jan 20	503.9	−4.7	16.452 ± 0.033	16.937 ± 0.027	16.785 ± 0.013	17.052 ± 0.026	17.039 ± 0.019	17.353 ± 0.033	LCO
2019 Jan 20	504.3	−4.3	...	16.817 ± 0.052	16.908 ± 0.162	17.262 ± 0.050	...	17.423 ± 0.052	TNT
2019 Jan 21	505.3	−3.3	...	16.623 ± 0.013	16.768 ± 0.018	17.014 ± 0.030	16.901 ± 0.029	17.328 ± 0.038	TNT
2019 Jan 21	505.2	−3.4	16.882 ± 0.08	0.7 m
2019 Jan 22	506.2	−2.4	16.777 ± 0.063	0.7 m
2019 Jan 23	506.8	−1.8	16.122 ± 0.074	...	16.613 ± 0.039	16.883 ± 0.051	LCO
2019 Jan 23	507.3	−1.3	...	16.654 ± 0.036	16.699 ± 0.022	16.991 ± 0.034	16.821 ± 0.034	17.187 ± 0.042	LCO
2019 Jan 24	507.8	−0.8	16.252 ± 0.075	16.731 ± 0.031	16.532 ± 0.015	16.669 ± 0.027	16.676 ± 0.022	17.215 ± 0.022	LCO
2019 Jan 25	508.1	−0.6	16.673 ± 0.024	...	17.037 ± 0.015	LJT
2019 Jan 25	508.3	−0.3	16.015 ± 0.020	16.825 ± 0.031	16.655 ± 0.019	16.616 ± 0.101	16.782 ± 0.022	17.027 ± 0.0272	LJT,TNT,0.7 m
2019 Jan 25	508.8	0.1	16.199 ± 0.051	16.740 ± 0.026	16.565 ± 0.017	16.685 ± 0.028	16.654 ± 0.023	17.003 ± 0.055	LCO
2019 Jan 28	511.4	2.7	16.732 ± 0.143	0.7 m
2019 Jan 28	511.8	3.1	16.331 ± 0.028	17.156 ± 0.017	...	16.749 ± 0.0153	16.646 ± 0.010	...	DFOT
2019 Jan 30	513.1	4.5	16.786 ± 0.085	ST
2019 Feb 1	515.7	7.1	17.334 ± 0.049	17.447 ± 0.026	17.281 ± 0.009	17.307 ± 0.019	17.237 ± 0.011	17.430 ± 0.021	LCO
2019 Feb 2	516.3	7.6	...	17.547 ± 0.016	17.257 ± 0.011	17.655 ± 0.022	17.532 ± 0.016	17.696 ± 0.013	TNT
2019 Feb 4	518.4	9.8	...	18.275 ± 0.016	17.847 ± 0.017	17.948 ± 0.014	ST
2019 Feb 4	518.8	10.2	18.262 ± 0.082	18.276 ± 0.029	17.921 ± 0.016	17.882 ± 0.025	17.835 ± 0.021	17.938 ± 0.030	LCO
2019 Feb 5	519.2	10.5	...	18.754 ± 0.031	...	17.885 ± 0.024	17.856 ± 0.017	...	ST
2019 Feb 6	520.3	11.7	...	18.862 ± 0.024	...	18.141 ± 0.025	18.479 ± 0.027	18.592 ± 0.033	ST
2019 Feb 8	523.4	14.8	19.787 ± 0.041	19.058 ± 0.027	...	18.316 ± 0.031	18.900 ± 0.001	18.808 ± 0.052	HCT
2019 Feb 9	524.4	15.7	...	19.224 ± 0.069	...	18.598 ± 0.029	18.911 ± 0.037	19.091 ± 0.033	ST
2019 Feb 12	527.0	18.4	...	19.487 ± 0.053	19.169 ± 0.037	18.946 ± 0.043	19.012 ± 0.048	19.136 ± 0.075	LCO
2019 Feb 20	535.2	26.6	20.037 ± 0.218	20.287 ± 0.115	TNT
2019 Feb 21	536.2	27.6	20.228 ± 0.214	TNT
2019 Feb 23	538.1	29.5	20.265 ± 0.312	TNT
2019 Mar 2	544.3	36.2	...	21.231 ± 0.274	20.726 ± 0.138	20.526 ± 0.178	21.032 ± 0.305	21.096 ± 0.215	LCO

Note.

^a With respect to $JD_{\max} = 2458508.65$.

Table 2
Log of Spectroscopic Observations of SN 2019uo

Date	JD – 2458000	Phase ^a	Telescope	Instrument	Range (Å)
2019 Jan 19	503.4	–5.2	2.4 m LJT	YFOSC	3500–8800
2019 Jan 20	503.9	–4.7	2.0 m FTN	FLOYDS	3200–9000
2019 Jan 21	504.9	–3.7	2.0 m FTN	FLOYDS	3200–9000
2019 Jan 23	506.9	–1.7	2.0 m FTN	FLOYDS	3200–9000
2019 Jan 24	508.3	–0.3	2.4 m LJT	YFOSC	3500–8800
2019 Jan 28	512.4	3.8	2.0 m FTN	FLOYDS	3200–9000
2019 Feb 5	519.9	11.3	2.0 m FTN	FLOYDS	3200–9000
2019 Feb 8	523.8	15.2	2.2 m China	BFOSC	4000–10000
2019 Feb 14	529.2	20.6	2.4 m LJT	YFOSC	3500–8800

Note.

^a With respect to $JD_{\max} = 2458508.65$.

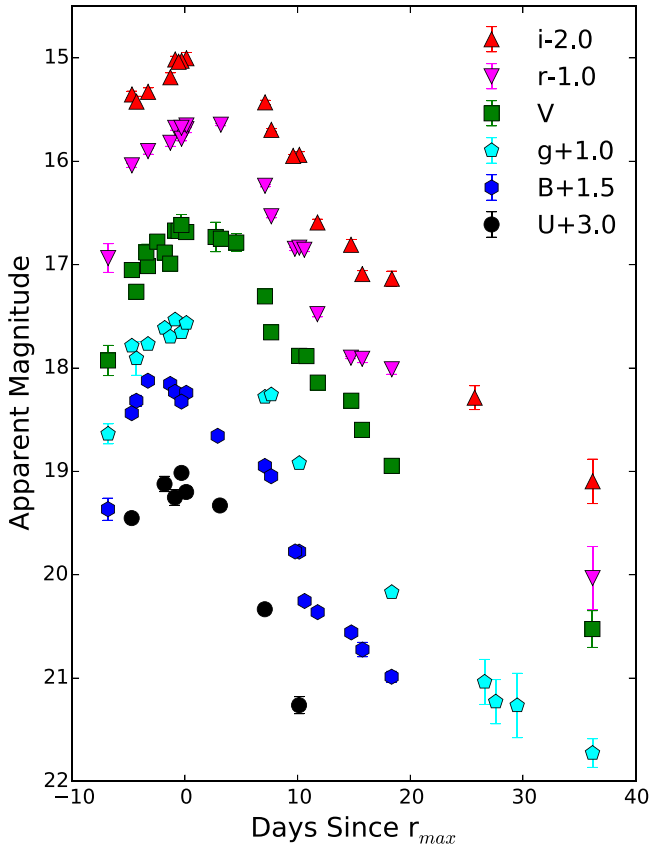


Figure 1. *UBVgr* light-curve evolution of SN 2019uo.

massive binaries (Foley et al. 2007). However, a low-mass progenitor has been suggested for PS1-12sk, which occurred in a non-star-forming host (Sanders et al. 2013; Hosseinzadeh et al. 2019)—unlikely for a CCSN ($\leq 0.2\%$; Hakobyan et al. 2012). A very recent study by Sun et al. (2020) for SNe 2006jc and 2015G implies an interacting binary progenitor scenario, based on late time UV/optical *Hubble Space Telescope* (*HST*) images.

In this paper we study the evolution of one such type Ibn SN 2019uo which was discovered on 2019 January 17.8 UT (JD 2458501.3) by Koichi Itagaki at R.A. = $12^h02^m36^s.5$, Decl. = $+41^\circ03'42''$ (J2000.0). The SN location is $0''.4$ east and $27''.2$ north of the center of the galaxy UGC 7020 at a

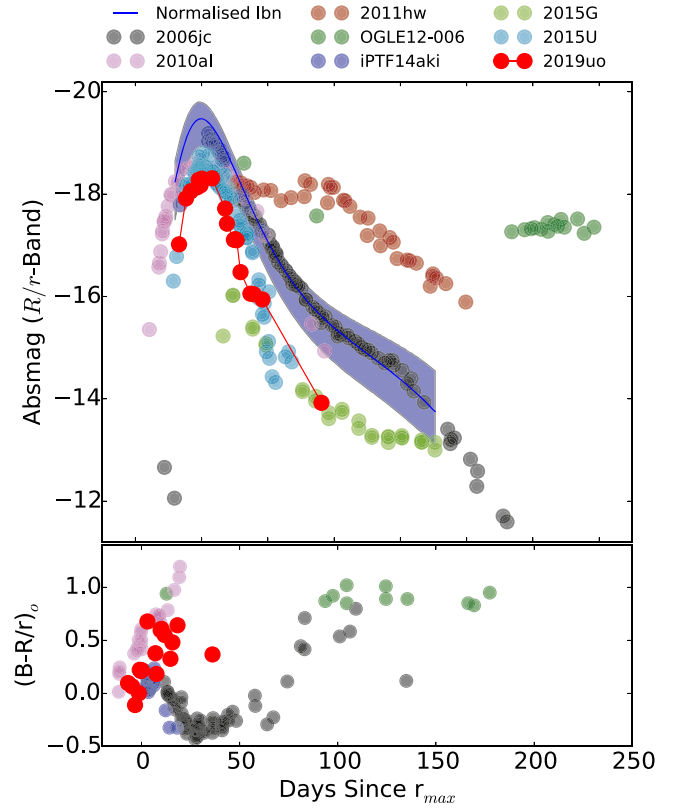


Figure 2. *R/r*-band absolute magnitude light curve and *B–R/r* color curve of SN 2019uo. The comparison sample includes SNe 2006jc (Foley et al. 2007; Pastorello et al. 2007), 2010al (Pastorello et al. 2015b), OGLE-SN-006 (Pastorello et al. 2015d), 2011hw (Pastorello et al. 2015b), iPTF14aki (Hosseinzadeh et al. 2017), 2015U (Shivvers et al. 2016; Hosseinzadeh et al. 2017), and 2015G (Hosseinzadeh et al. 2017).

redshift of 0.020454 (Zhang et al. 2019). SN 2019uo was classified on 2019 January 19.9 UT as a SN II (Zhang et al. 2019) with the spectrum obtained with the Yunnan Faint Object Spectrograph and Camera (YFOSC) mounted on the 2.4 m LiJiang Telescope (LJT) at Yunnan Observatory (YNAO). Zhang et al. (2019) reported that the spectrum depicted a blue continuum and highly ionized “flash features” such as N V, He II, and O V. However, this classification of type II SN was modified later by Fremling et al. (2019) and SN 2019uo was classified as a type Ibn. Prominent narrow emission lines of He I in the initial spectra of SN 2019uo

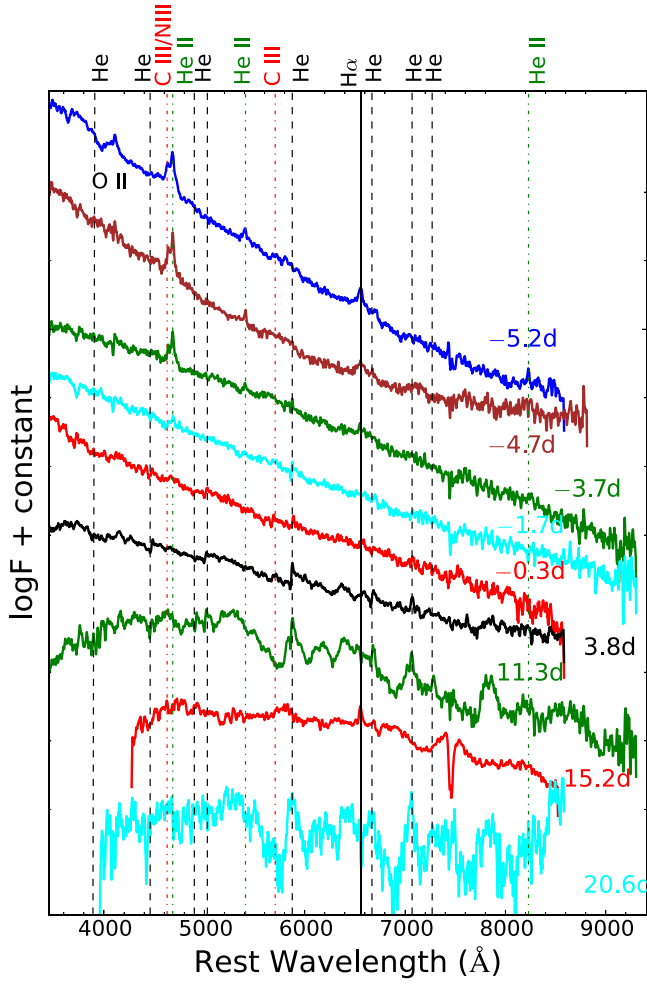


Figure 3. Spectral evolution of SN 2019uo from -5.2 to 20 days post r_{\max} . Prominent He features are seen in the early spectra. Flash ionization signatures of He II, C III, and N III are also seen.

indicating a P-cygni velocity of 650 km s^{-1} justified the type Ibn classification. SN 2019uo is the second SN Ibn to show these features after SN 2010al. Adopting $H_0 = 73 \text{ km s}^{-1} \text{ Mpc}^{-1}$, we obtain a luminosity distance of 88.8 Mpc for SN 2019uo. The Milky Way extinction along the line of sight of SN 2019uo is $A_V = 0.035 \text{ mag}$ (Schlafly & Finkbeiner 2011). For estimating the extinction along the line of sight within host galaxy, we estimate equivalent widths of the NaID line in the first three spectra of SN 2019uo. Using the formulation by Munari & Zwitter (1997) and Poznanski et al. (2012), we estimate $A_V = 0.2517 \text{ mag}$. This estimate also brings the $B-V$ colors of SN 2019uo into close agreement with SNe 2006jc and 2010al. Thus, we adopt a total $A_V = 0.287 \text{ mag}$. The temporal and spectral evolution of SN 2019uo and the detailed modeling of the bolometric light curve is discussed in the sections to follow.

2. Data Acquisition and Reduction

We observed SN 2019uo with Las Cumbres Observatory (LCO) in the $UBVgri$ filters from ~ 2 to 106 days after discovery. Augmenting the LCO data, photometric observations in $UBVRi/ugri$ were also taken with 0.7 m BITRAN-CCD Imaging System located in Japan; 0.8 m Tsinghua-NAOC Telescope (TNT), Xinglong Observatory, China; 1.04 m Sampurnanand Telescope (ST); 1.30 m Devasthal Fast Optical Telescope (DFOT), ARIES,

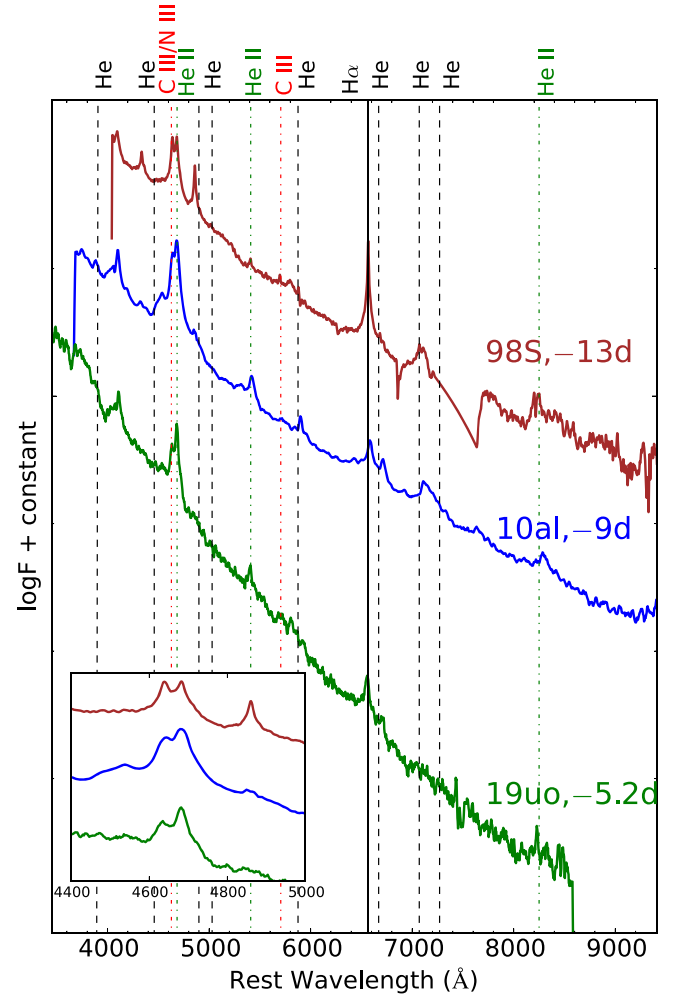


Figure 4. Spectral comparison of SN 2019uo at -5.2 days to SNe 1998S (Fassia et al. 2001) and 2010al (Pastorello et al. 2015b). Prominent flash ionization features are marked.

India; 2.00 m Himalayan Chandra Telescope (HCT), IAO, Hanle, India and Lijiang 2.4 m Telescope (LJT), YNAO, China. We performed image subtraction using High Order Transform of point-spread function (PSF) AND Template Subtraction (HOT-PANTS;¹⁸ Becker 2015). The instrumental magnitudes were estimated using IRAF¹⁹ (Tody 1986, 1993) and DAOPHOT²⁰ (Stetson 1987). The LCO photometry was done using lcogetsnpipe²¹ (see Valenti et al. 2011, 2016) on the difference images. The instrumental SN magnitudes were calibrated using the standard magnitudes of a number of local stars in the SN field obtained from the Sloan Digital Sky Survey (SDSS) catalog for the gri bands and the Landolt standard fields taken on the same night by the same instrument as the science images for UBV . Wherever required, the RI magnitudes were converted to ri using the equations of Jordi et al. (2006). The photometry of SN 2019uo is presented in Table 1.

The spectroscopic observations were taken at nine epochs spanning up to ~ 88 days after discovery. The 1D wavelength-

¹⁸ <https://github.com/acbecker/hotpants>

¹⁹ Image Reduction and Analysis Facility.

²⁰ Dominion Astrophysical Observatory Photometry.

²¹ <https://github.com/svalenti/lcogetsnpipe>

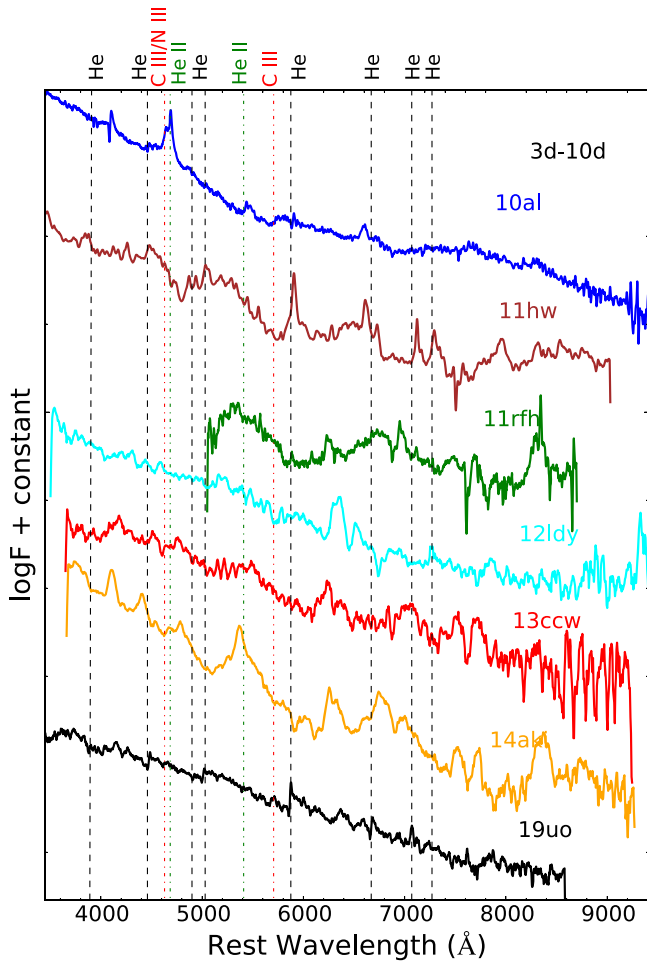


Figure 5. Comparison of the spectrum of SN 2019uo to other SNe Ibn. SN 2019uo and SN 2010al show distinct narrow P-cygni He I spectroscopic features. The data for this are taken from SNe 2010al (Pastorello et al. 2015a), 2011hw (Pastorello et al. 2015a), PTF11rfh (Hosseinizadeh et al. 2017), PTF12ldy (Hosseinizadeh et al. 2017), LSQ13ccw (Pastorello et al. 2015b), and iPTF14aki (Hosseinizadeh et al. 2017).

and flux-calibrated spectra were extracted using the floydsspec pipeline (Valenti et al. 2014) for the LCO data. Spectroscopic data reduction of the 2.2 m and 2.4 m telescopes was done using the APALL task in IRAF followed by wavelength and flux calibration. The slit loss corrections were done by scaling the spectra to the photometry. Finally, the spectra were corrected for the heliocentric redshift of the host galaxy. The log of spectroscopic observations is given in Table 2.

3. Photometric Evolution of SN 2019uo

The complete multiband light curve of SN 2019uo is shown in Figure 1. With our available observations, we were able to trace the epoch of maximum in all the bands. The date of maximum and its brightness were determined by fitting a cubic spline to the *UBVgr* light curves. The maximum in *r*-band occurred on JD 2458508.6 \pm 0.5 at an apparent magnitude of 16.66 \pm 0.03 mag. The errors reported are obtained from interpolated measurements around the peak. We use days since *r*-maximum (r_{\max}) as a reference epoch throughout the paper. Assuming that the discovery date is close to explosion, we estimated a rise time of 8.7 \pm 1.3 days. This is similar to

iPTF14aki and iPTF15akq (see Table 4; Hosseinizadeh et al. 2017).

The *r*-band light curve, between 0 and 36 days, decays with a rate of 0.126 ± 0.005 mag day $^{-1}$. The *g*, *B*, *V*, and *i* bands follow approximately the same decline rate. The sample of SNe Ibn in Hosseinizadeh et al. (2017) are fast-evolving with a typical decline rate of 0.1 mag day $^{-1}$ during the first month post-maximum. SN 2019uo follows the same decline rate.

Figure 2 shows the absolute magnitude light curve of SN 2019uo along with other SNe Ibn after correcting for distance and extinction. The peak *r*-band absolute magnitude of SN 2019uo is -18.30 ± 0.24 mag, which is at the fainter end of the SN Ibn sample. The blue band in Figure 2 shows the average light curve (comprising of 95% of the SN Ibn data) of SNe Ibn taken from Hosseinizadeh et al. (2017). The average light curve was generated by using a Gaussian process to fit a smooth curve to the combined light curves on the sample of Hosseinizadeh et al. (2017). The fit was performed in log-log space to ensure consistency and smoothness between the early and late time light curves. The average light curve, thus, generated also uses the Gaussian process to fit positive and negative residuals. Note that SN 2019uo is ~ 1.2 mag fainter than the normalized SNe Ibn light curve.

We compare the *B*–*R*/*r* color evolution of SN 2019uo with a number of SNe Ibn, which usually show heterogeneity in their color evolution. The *B*–*r* color of SN 2019uo increases up to 0.64 mag ~ 20 days post r_{\max} , subsequently becoming blue at ~ 36 days. Similarly, for SN 2010al and iPTF14aki the *B*–*r* color increases up to ~ 1 mag, ~ 30 days post R_{\max} . Thus, SN 2019uo shows a color evolution similar to SN 2010al and iPTF14aki. At similar epochs, the color evolution of SN 2006jc was extremely blue (-0.5 mag). SN 2006jc then shows an overall flatter color evolution. The early blue color are typical of SN Ibn (Pastorello et al. 2016). The transition to redder colors for SNe 2019uo and 2010al places their behavior between SNe Ib and most extreme SNe Ibn. SN 2006jc (Pastorello et al. 2007) and OGLE-2012-SN-006 (Pastorello et al. 2015d) show redder colors post 50 days.

4. Spectral Evolution

The spectral evolution of SN 2019uo from -5.2 days to 20.6 days post-maximum is displayed in Figure 3. The early spectral sequence shows a unique blue continuum similar to SN 2010al. Blackbody fits to the first three spectra (-5.2 , -4.7 , and -3.7 days) show that the photospheric temperature varies between 13,000 and 10,000 K. A very narrow H emission line (≤ 137 km s $^{-1}$; unresolved) in the early spectrum of SN 2019uo is most likely due to interstellar gas in the host galaxy. Prominent emission features in the first three spectra (-5.2 to -3.7 days) of SN 2019uo are seen around ~ 4660 Å. The emission components are double-peaked, with the blue component peaking at 4643 Å and the red component peaking at 4682 Å. The red component at 4682 Å is due to He II at 4686 Å, whereas the blue component arises from a blend of C III 4648 Å and N III 4640 Å. Another interesting feature is the possible identification of a doubly ionized C III feature at 5696 Å. Pastorello et al. (2015a) interpreted these as flash ionization signatures in a He-rich CSM (also see Gal-Yam 2014). Although C III features were found in PTF12ldy and iPTF15ul (Hosseinizadeh et al. 2017), SN 2010al is the only previous SN Ibn where flash ionization signatures of C III

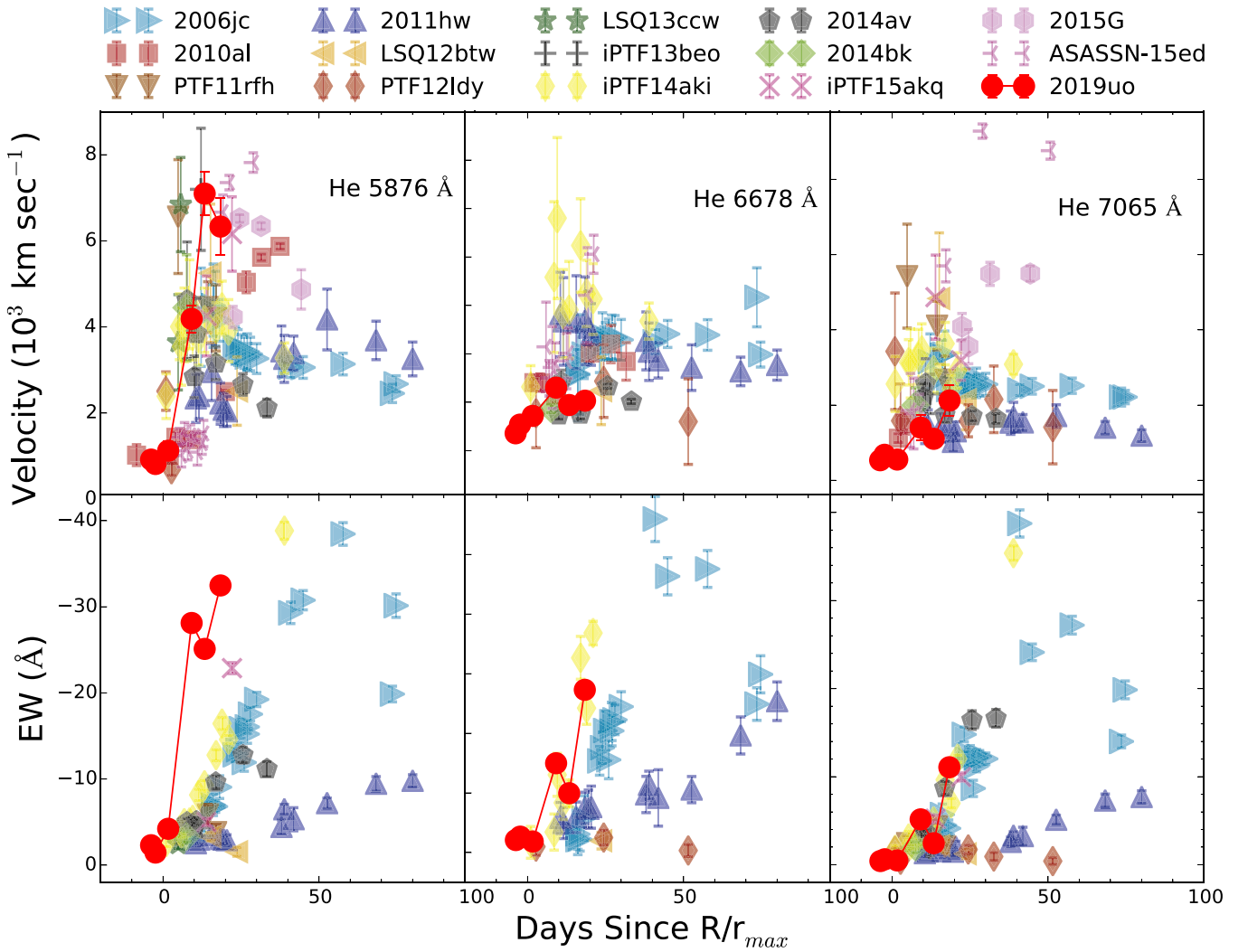


Figure 6. Evolution of line velocities and equivalent widths of He I emission lines is shown in the top and bottom panels, respectively. The data for this are taken from SNe 2006jc (Foley et al. 2007; Pastorello et al. 2008), 2010al (Pastorello et al. 2015a), 2011hw (Pastorello et al. 2015a), PTF11rfrh (Hossein-zadeh et al. 2017), LSQ12btw (Pastorello et al. 2015b), OGLE12-006 (Pastorello et al. 2015d), PTF12ldy (Hossein-zadeh et al. 2017), iPTF13beo (Gorbikov et al. 2014), LSQ13ccw (Pastorello et al. 2015b), iPTF14aki (Hossein-zadeh et al. 2017), 2014av (Pastorello et al. 2016), 2014bk (Pastorello et al. 2016), iPTF15akq (Hossein-zadeh et al. 2017), ASASSN-15ed (Pastorello et al. 2015c), and 2015G (Hossein-zadeh et al. 2017).

and He II, typical of SNe II, are both seen. Cooke et al. (2010) and Silverman et al. (2010) identified such lines to be originating from a WR wind, previously noted in SNe IIn (e.g., SN 1998S; Fassia et al. (2001) and SN 2008fq; Taddia et al. 2013). We also identify a He II 5411 Å feature with a velocity of 1483 km s^{-1} at -5.2 days. In the spectrum at -5.2 days, we see a deep absorption feature at ~ 4000 Å and a small dip around 8200 Å, which is likely due to the presence of O II and He II features, respectively.

Figure 4 shows the spectra of SNe 1998S (type IIn) and 2010al (type Ibn) in comparison with SN 2019uo. These two SNe have previously shown flash ionization signatures. While the spectrum of SN 2010al shows C III features around 4650 Å only, SN 2019uo shows C III features around 4650 Å and at 5696 Å. The inset in Figure 4 highlights these features.

As the SN evolves further (3.8 days), the narrow He I P-cygni feature is superimposed on a broader base (the continuum is not flat). The flash ionization spectral features vanish completely during this epoch. From 11 to 21 days, features of Ca II, Si II, and Na ID also start developing (see

Figure 3). Figure 5 shows the comparison of SN 2019uo with a group of SNe Ibn between 3 and 10 days after peak. The He I 5876 Å feature of SN 2019uo is similar to that identified in SN 2010al. However, the He I P-cygni feature of SN 2019uo is narrower, and is superimposed over a broader emission line. On the other hand, the He I P-Cygni profile in SN 2010al is over a flat continuum. Flash ionization signatures in SN 2010al are still visible at this phase, but these features have vanished in SN 2019uo. The line evolution of SN 2019uo shows that it belongs to the “P-cygni” subclass (following the interpretation of Hossein-zadeh et al. 2017). The P-cygni He I features are narrow but gradually broaden with time. The physical explanation behind the origin of the “P-cygni” subclass could be a shell of He around the progenitor star surrounded by a dense CSM. As the optically thick shell is lit by the explosion, the narrow P-cygni features transition to broader emission as the shell is swept up by the SN ejecta. The viewing angle dependence could also affect this scenario; if the CSM is asymmetric and we have a He rich torus, then P-cygni features would only be visible if the system is viewed edge-on, while

Table 3
Parameters of the ^{56}Ni Model

M_{ej} (M_{\odot})	M_{Ni} (M_{\odot})	v_{sc0} (10^9 cm s^{-1})	$\kappa_{\gamma, \text{Ni}}$ ($\text{cm}^2 \text{ g}^{-1}$)	t_{expl}^a (days)	χ^2/dof
$0.81^{+0.19}_{-0.18}$	$0.24^{+0.02}_{-0.02}$	$2.24^{+0.19}_{-0.30}$	$0.01^{+0.00}_{-0.00}$	$-9.21^{+0.28}_{-0.30}$	6.67/19

Notes. Uncertainties are 1σ .

^a The value of t_{expl} is with respect to r_{max} .

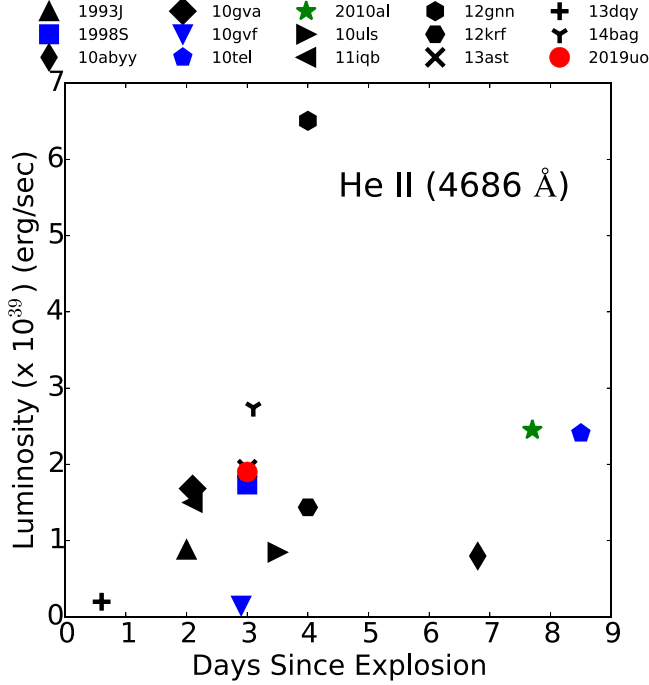


Figure 7. He II luminosity of a sample of SNe II, IIn, and Ibn (Khazov et al. 2016) with flash ionization signatures. Blue symbols: type IIn; black symbols: type II (IIb, IIP, and IIL); red symbols: type Ibn.

emission features can be seen only if it is viewed face-on. However, this scenario was questioned by Karamahmetoglu et al. (2019) who suggested that He I line fluxes are largely dependent on density, temperature, and optical depths. Karamahmetoglu et al. (2019) suggest that dominance of emission at late phases is not because they are optically thin, but because they lack other lines to branch into it. He ionization and recombination are mostly caused by UV and X-ray, occurring at shock boundary, deep in interacting regions. Even though most of the emission and the electron scattering are produced by the ionized region outside the shock, P-cygni features usually originate from optical depths ≤ 1 . X-rays penetrating further into the P-cygni producing regions will fill in the absorption and lead to emission features. Thus, this provides an alternative scenario to the transitioning of P-cygni to emission features of He I lines for SNe Ibn.

We measured the expansion velocities and equivalent widths (EWs) of three neutral He lines (5876, 6678, and 7065 Å), wherever visible. We fit the emission lines of He I using a Gaussian on a linear continuum. The EW is estimated through the integral of the flux normalized to the local continuum. We do not measure the EW of the P-cygni lines. The velocities

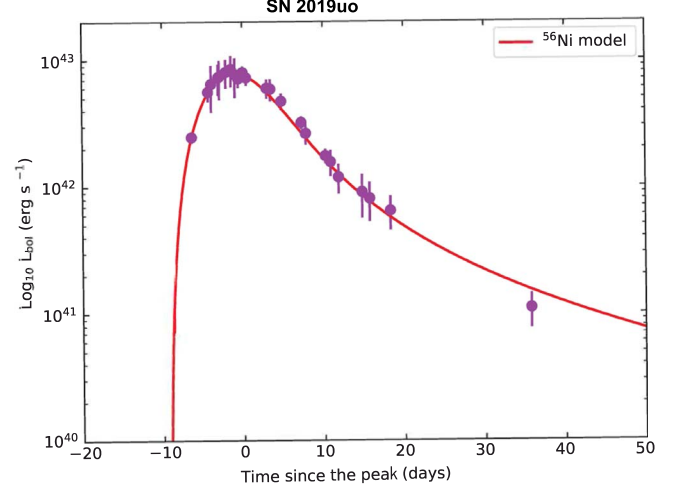


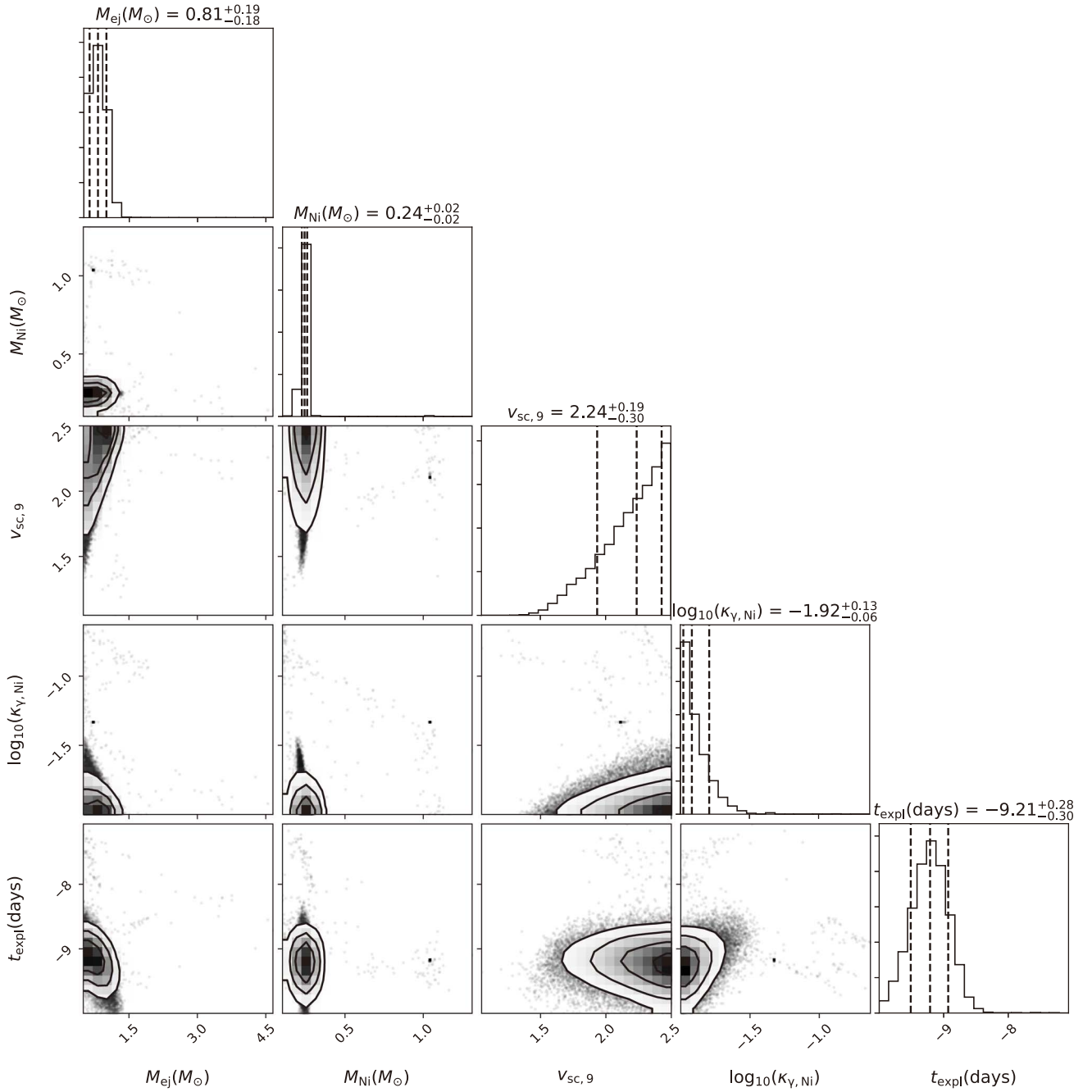
Figure 8. Best-fit light curves of SN 2019uo using a ^{56}Ni model.

reported are estimated from the absorption minima of P-cygni profiles. Figure 6 shows the evolution of velocity and EW for a sample of SNe Ibn taken from Hosseinzadeh et al. (2017) with time. We see that both the line velocities and EW of the He lines gradually increase with time and the velocity estimates of SN 2019uo lie in the lower range of SNe Ibn. However, SN 2019uo shows a faster evolution in line velocities, reaching broader emission profiles as seen in the P-cygni subclass (Hosseinzadeh et al. 2017) while the emission subclass shows very little velocity evolution.

To ascertain the origin of the SNe Ibn, we collected a sample of 12 SNe II (including SNe IIb and IIP, IIn) and Ibn from Khazov et al. (2016) that showed signatures of flash ionization within 10 days of explosion. Since the H lines are usually contaminated by the host galaxy, we selected the relatively unblended He II 4686 Å line. Since the He II lines are much narrower than lines from the SN ejecta, they can serve as a good tool for probing the flash-ionized CSM. When measuring the luminosities, we removed the continuum by fitting a linear function. Figure 7 shows that the typical luminosity of the He II line for SN 2019uo is similar to the type IIn SNe 1998S and PTF13ast.

5. Modeling the Bolometric Light Curve of SN 2019uo

To construct the bolometric light curve of SN 2019uo, the measured flux values were corrected for distance and reddening as given in Section 1. Spectral energy distributions (SEDs) were constructed accounting for the flux coverage between UV to IR bands using the *SuperBol* (Nicholl 2018) code. The lack of UV and NIR data was supplemented by extrapolating the

**Figure 9.** Corner plot of the ^{56}Ni model displaying covariance of estimated parameters.**Table 4**
Parameters of the CSI Model and the CSI Plus ^{56}Ni Model. The Uncertainties Are 1σ

	s	E_{SN} (10^{51} erg)	M_{ej} (M_{\odot})	M_{Ni} (M_{\odot})	M_{CSM} (M_{\odot})	$\rho_{\text{CSM, in}}$ (10^{-12} g cm^{-3})	$R_{\text{CSM, in}}$ (10^{14} cm)	ϵ	x_0	$\kappa_{\gamma, \text{Ni}}$ ($\text{cm}^2 \text{g}^{-1}$)	$t_{\text{expl}}^{\text{a}}$ (days)	χ^2/dof
CSI	2	$0.87^{+0.06}_{-0.04}$	$8.83^{+0.71}_{-0.99}$...	$0.40^{+0.04}_{-0.03}$	$3.34^{+3.33}_{-1.72}$	$1.76^{+0.91}_{-0.55}$	$0.11^{+0.01}_{-0.01}$	$0.35^{+0.08}_{-0.10}$...	$-7.24^{+0.09}_{-0.08}$	3.95/16
CSI	0	$0.40^{+0.31}_{-0.14}$	$13.51^{+3.91}_{-5.19}$...	$1.28^{+0.41}_{-0.44}$	$0.15^{+0.12}_{-0.04}$	$19.05^{+6.66}_{-7.98}$	$0.51^{+0.29}_{-0.25}$	$0.67^{+0.20}_{-0.22}$...	$-7.89^{+0.07}_{-0.07}$	13.44/16
CSI+ ^{56}Ni	2	$1.67^{+0.18}_{-0.23}$	$15.99^{+2.25}_{-2.98}$	$0.01^{+0.003}_{-0.002}$	$0.41^{+0.08}_{-0.07}$	$20.96^{+4.73}_{-4.83}$	$8.04^{+1.49}_{-1.39}$	$0.64^{+0.14}_{-0.12}$	$0.51^{+0.25}_{-0.19}$	$0.95^{+10.15}_{-0.88}$	$-6.42^{+0.00}_{-0.00}$	2.79/14
CSI+ ^{56}Ni	0	$1.78^{+0.13}_{-0.19}$	$16.30^{+2.09}_{-2.72}$	$0.01^{+0.003}_{-0.002}$	$0.73^{+0.12}_{-0.11}$	$25.05^{+2.75}_{-3.58}$	$14.16^{+1.85}_{-2.00}$	$0.71^{+0.12}_{-0.12}$	$0.43^{+0.22}_{-0.14}$	$0.90^{+10.40}_{-0.82}$	$-6.40^{+0.00}_{-0.00}$	3.17/14

Note.^a The value of t_{expl} is with respect to r_{max} .

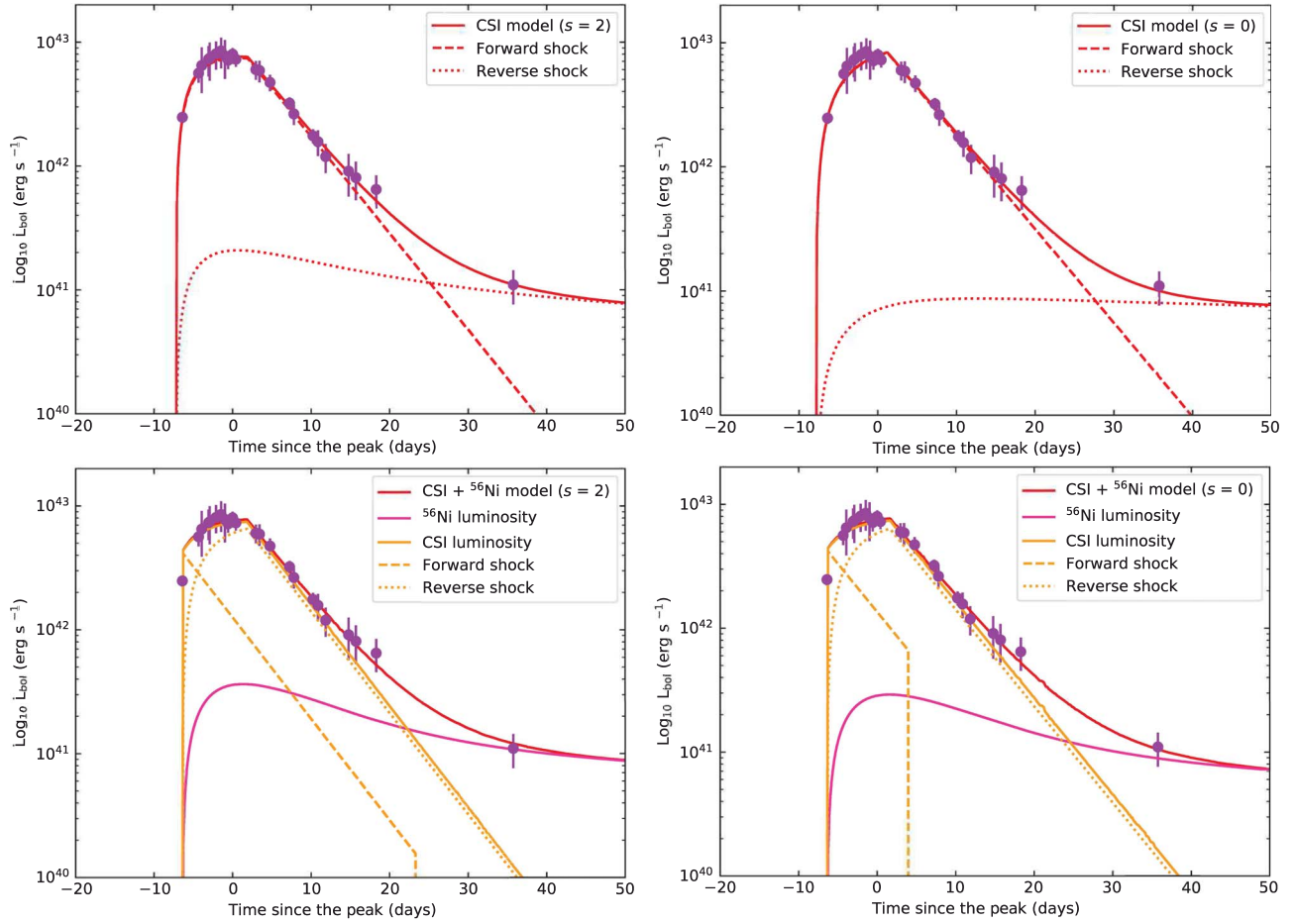


Figure 10. Best-fit light curves of SN 2019uo fitted with a CSI model and a combination of ^{56}Ni and CSI. The forward shocks, reverse shocks, and ^{56}Ni models are plotted with different lines.

SEDs using the blackbody approximation and direct integration method as described in Lusk & Baron (2017). A linear extrapolation was performed in the UV regime at late times. The estimated peak bolometric luminosity of SN 2019uo is $8.9 \times 10^{42} \text{ erg s}^{-1}$. We used different models to fit the bolometric light curve at a fixed optical opacity of $0.1 \text{ cm}^2 \text{ g}^{-1}$. A Markov Chain Monte Carlo (MCMC) technique was used to obtain the best-fit parameters.

^{56}Ni model: Assuming that the peak bolometric luminosity is powered by the decay of ^{56}Ni to ^{56}Co , we fit the bolometric light curve using ^{56}Ni model (Arnett 1982, 1980). The parameters of the ^{56}Ni model are the ejecta mass M_{ej} , the initial scale velocity of the ejecta v_{sc0} , the ^{56}Ni mass M_{Ni} , the gamma-ray opacity of ^{56}Ni decay photons $\kappa_{\gamma, \text{Ni}}$ and explosion time t_{expl} . The initial kinetic energy of the ejecta is neutrino-driven and is considered to be $E_k = 0.3 M_{\text{ej}} v_{\text{sc0}}^2$. The best-fit parameters are tabulated in Table 3 and the best-fit model is displayed in Figure 8. The corner plot showing the covariance of the estimated parameters is represented in Figure 9. We note that the ^{56}Ni mass obtained from the powering mechanism of Arnett (1982) are in concordance with the values quoted for several stripped envelope SNe (Lyman et al. 2016; Prentice et al. 2016, 2019). Although the ^{56}Ni mass inferred from the model is $\sim 0.24 M_{\odot}$ which is comparable to that of normal CCSNe, the opacity for the gamma-ray $\kappa_{\gamma, \text{Ni}}$ emitted from the cascade decay of ^{56}Ni is $0.01 \text{ cm}^2 \text{ g}^{-1}$, which is

significantly smaller than the canonical lower limit which is $0.025\text{--}0.027 \text{ cm}^2 \text{ g}^{-1}$. Therefore, the ^{56}Ni model is not a good model in explaining the light curve of SN 2019uo and other models must be employed.

The circumstellar interaction (CSI) model and the ^{56}Ni + CSI model: The narrow He emission lines appearing in the spectra of SN 2019uo indicate a potential source of CSI with a nearby He-rich shell. Thus, the nearby He-rich wind or shell surrounding the progenitor could be the essential powering source of the bolometric light curve of SN 2019uo. We take into account the ejecta-CSM interaction model (i.e., the CSI model; Chevalier 1982; Chevalier & Fransson 1994; Chugai & Danziger 1994; Ginzburg & Balberg 2012; Liu et al. 2018) and the ^{56}Ni + CSI model (Chatzopoulos et al. 2012). To fit the bolometric light curve of SN 2019uo, we adopt the formulation given in Wang & Li (2019).

The ejecta can be broadly distinguished into two zones: the inner part ($\rho_{\text{ej}} \propto r^{-\delta}$) and the outer part ($\rho_{\text{ej}} \propto r^{-n}$). The density profile of the CSM can typically be described as a power law where $\rho_{\text{CSM}} \propto r^{-s}$, where $s = 0$ corresponds to shells of the CSM and $s = 2$ corresponds to winds. Assuming $\delta = 1$ and $n = 10$, the adopted parameters of the CSM model are the energy of the SN (E_{SN}), the mass of the ejecta (M_{ej}), the mass of the CSM (M_{CSM}), the density of the innermost part of the CSM $\rho_{\text{CSM, in}}$, the radius of the innermost part of the ejecta

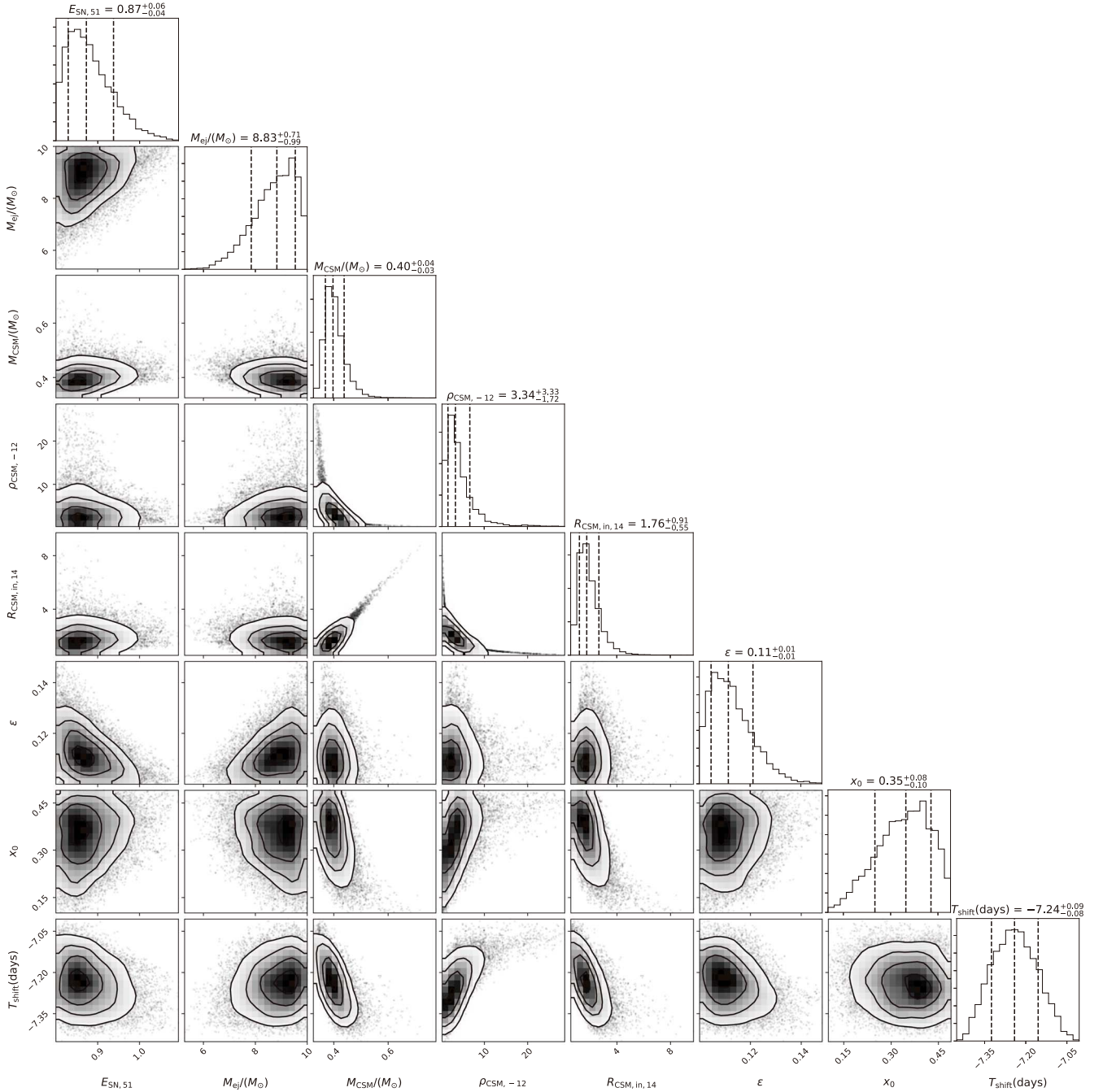


Figure 11. Corner plot of the CSI wind model displaying covariance of estimated parameters.

$R_{\text{CSM},\text{in}}$, the efficiency factor which converts kinetic energy to radiation (ϵ), the dimensionless x_0 parameter,²² and t_{expl} . Two additional parameters are used in the ^{56}Ni + CSI model: M_{Ni} and $\kappa_{\gamma,\text{Ni}}$. The best-fit parameters of the model are tabulated in Table 4 and the best-fit models are displayed in Figure 10. The corner plots describing covariance of the parameters are shown in Figures 11–14 respectively. The tabulated values of ejecta masses of the four models are reasonable if the progenitor is a WR star of mass $\sim 25 M_{\odot}$ and the metallicity is nearly solar (Crowther & Smartt 2007). We adopted the ^{56}Ni , CSI model, and the ^{56}Ni + CSI models to fit the bolometric light curve of SN 2019uo. The ^{56}Ni model provides a favorable fit to the light

curve, but this model cannot explain the He I emission lines present in the spectrum of SN 2019uo. These lines are likely generated because of the CSI. We therefore invoke CSI as the more favorable model to model light curve. For the CSI model, the estimated ejecta masses for $s = 0$ and $s = 2$ are $8.83^{+0.71}_{-0.99} M_{\odot}$ and $13.51^{+3.91}_{-5.19} M_{\odot}$ respectively. This model, however, did not take into account the role of ^{56}Ni . Using the combination of both ^{56}Ni + CSI, the estimated M_{ej} for $s = 0$ and $s = 2$ is $15.99^{+2.25}_{-2.98} M_{\odot}$ and $16.30^{+2.09}_{-2.72} M_{\odot}$, respectively, which are consistent with a WR progenitor scenario. The mass-loss rate is given by $\dot{M} = 4\pi v_w q$ (where $q = \rho_{\text{CSM},\text{in}} R_{\text{CSM},\text{in}}^2$). The velocity of the wind $v_w = 100\text{--}1000 \text{ km s}^{-1}$ for WR systems. Considering the wind CSI model ($s = 2$), we find that the estimated mass-loss rate lies between 0.195 and $1.95 M_{\odot} \text{ yr}^{-1}$,

²² $x \equiv \frac{r(t)}{R(t)}$, where $x \leq x_0$ and $x \geq x_0$ are inner and outer parts of the ejecta.

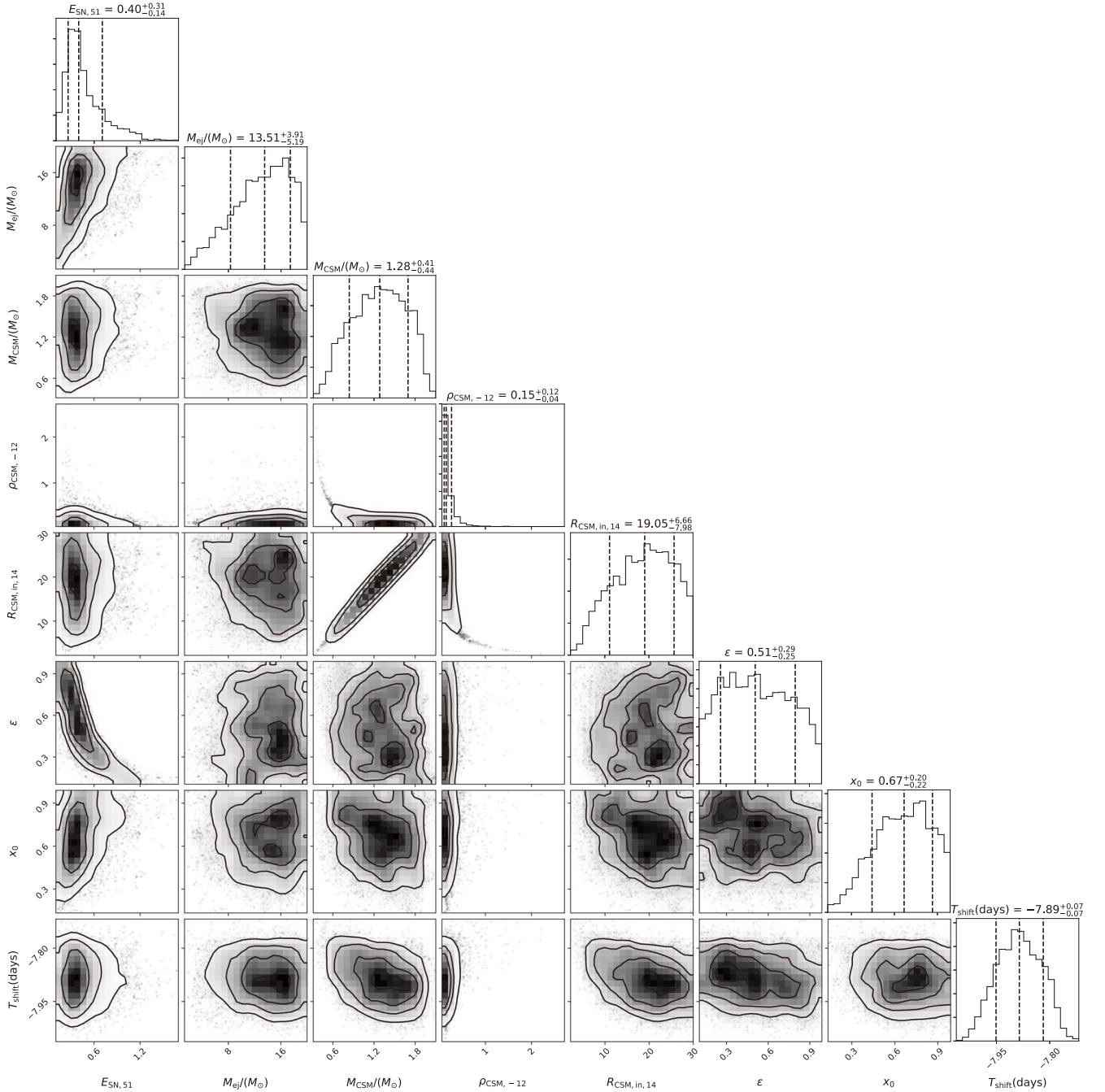


Figure 12. Corner plot of the CSI shell model displaying covariance of estimated parameters.

which is comparable with the values obtained for iPTF13z ($0.1\text{--}2 M_{\odot} \text{ yr}^{-1}$; Nyholm et al. 2017) and PS15dnp ($1\text{--}10 M_{\odot} \text{ yr}^{-1}$; Wang & Li 2019). Using the combination of ^{56}Ni +CSI model ($s = 2$), the estimated mass-loss rate lies between 25.5 and $255.4 M_{\odot} \text{ yr}^{-1}$ which is significantly higher than the value obtained for iPTF13z and PS15dnp, and this model can be excluded. Nevertheless, the ^{56}Ni +CSM shell is reasonable.

For the CSM shell and the ^{56}Ni + CSM shell model, the expelled shell masses prior to explosion are $\sim 1.3 M_{\odot}$ and $0.73 M_{\odot}$, respectively. The radius of the inner shell for the ^{56}Ni + CSI model, as seen from Table 4, is $14 \times 10^{14} \text{ cm}$ and the typical velocity of WR winds is between 100 and 1000 km s^{-1}

($10^{7-8} \text{ cm s}^{-1}$); so the time at which the shell is expelled prior to explosion is estimated to be between $1.4 \times 10^6 \text{ s}$ and $1.4 \times 10^7 \text{ s}$, i.e., between 163.8 and 1638.8 days.

6. Summary

In this paper, we present the photometric and spectral evolution of the type Ibn SN 2019uo. The typical light-curve decay rate of SNe Ibn is $\sim 0.1 \text{ mag day}^{-1}$ in all bands which is in agreement with the decline rates of the SNe Ibn discussed by Hosseinzadeh et al. (2017). The color evolution of SN 2019uo is similar to SN 2010al and iPTF14aki which places it between SNe Ib and SNe Ibn. This is in good agreement with the

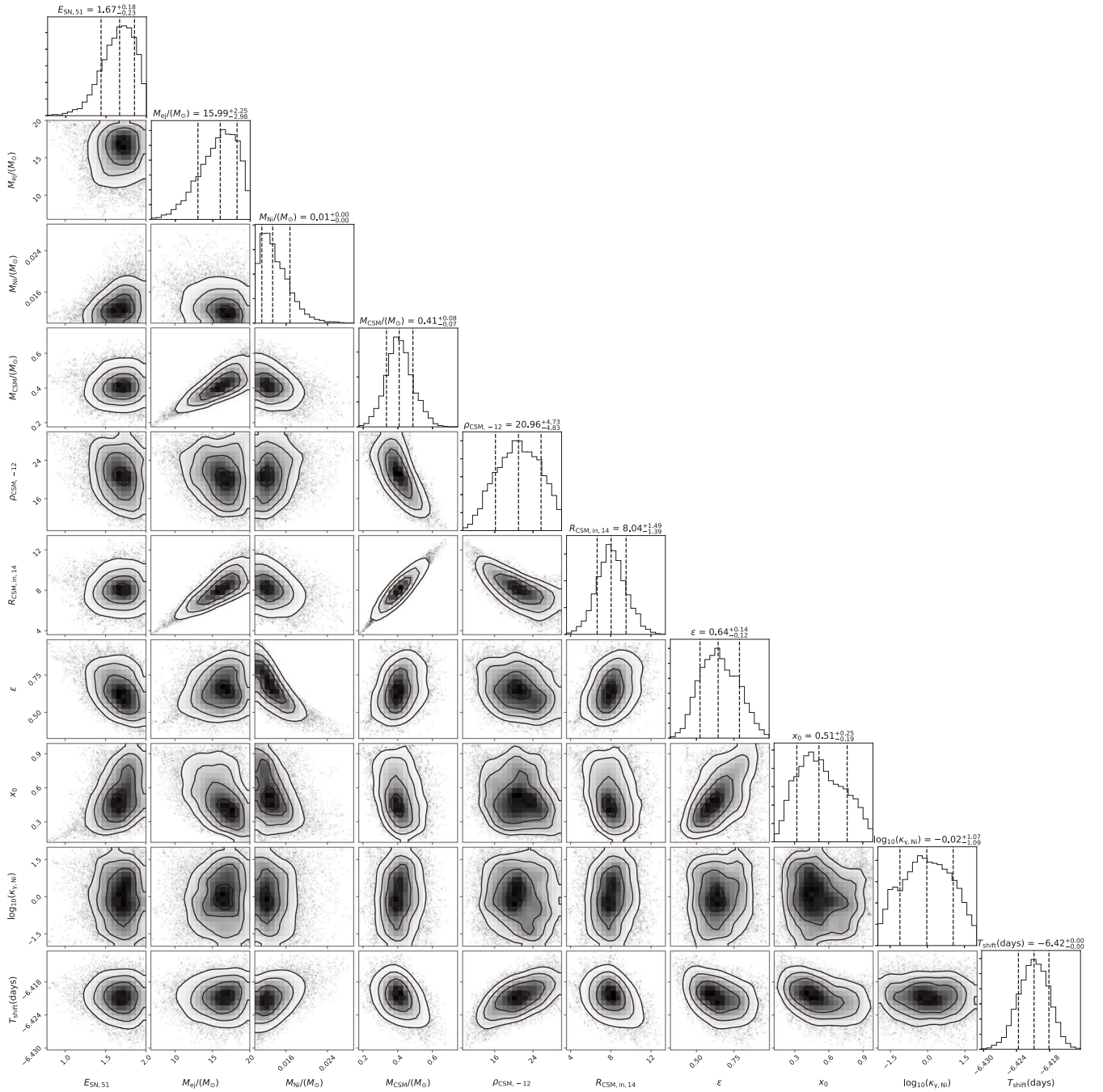


Figure 13. Corner plot of the ^{56}Ni + CSI wind model displaying covariance of estimated parameters.

P-cygni spectroscopic features that transition from narrow to broad, indicating a He-rich circumstellar shell around the progenitor star along with optically thick CSM (Hosseinizadeh et al. 2017). The absolute magnitude ($M_{\text{max}}^V = -18.30 \pm 0.24$ mag) indicates that SN 2019uo lies at the fainter end of the group. We fit the bolometric light curve of SN 2019uo with ^{56}Ni model. However, the ^{56}Ni model alone does not take into account the CSM interaction that is evident from the narrow emission lines in the spectra of SN 2019uo. Thus, we also fit the light curves with a CSI model and a ^{56}Ni + CSI model. The ^{56}Ni + CSI wind ($s = 2$) model can be excluded since an unrealistic value of mass-loss rate ($25.5\text{--}255.4 M_{\odot} \text{ yr}^{-1}$) is required and the ^{56}Ni + CSI shell model is reasonable. The

combination of ^{56}Ni + CSI shell well fits our observed light curve, with ejecta masses consistent with a WR star. The spectroscopic features of SN 2019uo indicate that it is the second SNe Ibn with flash ionization signatures. Prominent lines of He II, C III, and N III are detected in the spectra, similar to SN 2010al. SN 2019uo shows initial P-cygni He I features that broaden after 11 days post-maximum. This can originate from a He-rich shell around a progenitor surrounded by dense CSM, or it may be due to viewing angle dependency. This is also validated by the equivalent widths of He I features. Alternatively, P-cygni spectroscopic features usually originate from optical depths ≤ 1 . As X-rays penetrate into the P-cygni producing regions absorptions are filled leading to subsequent

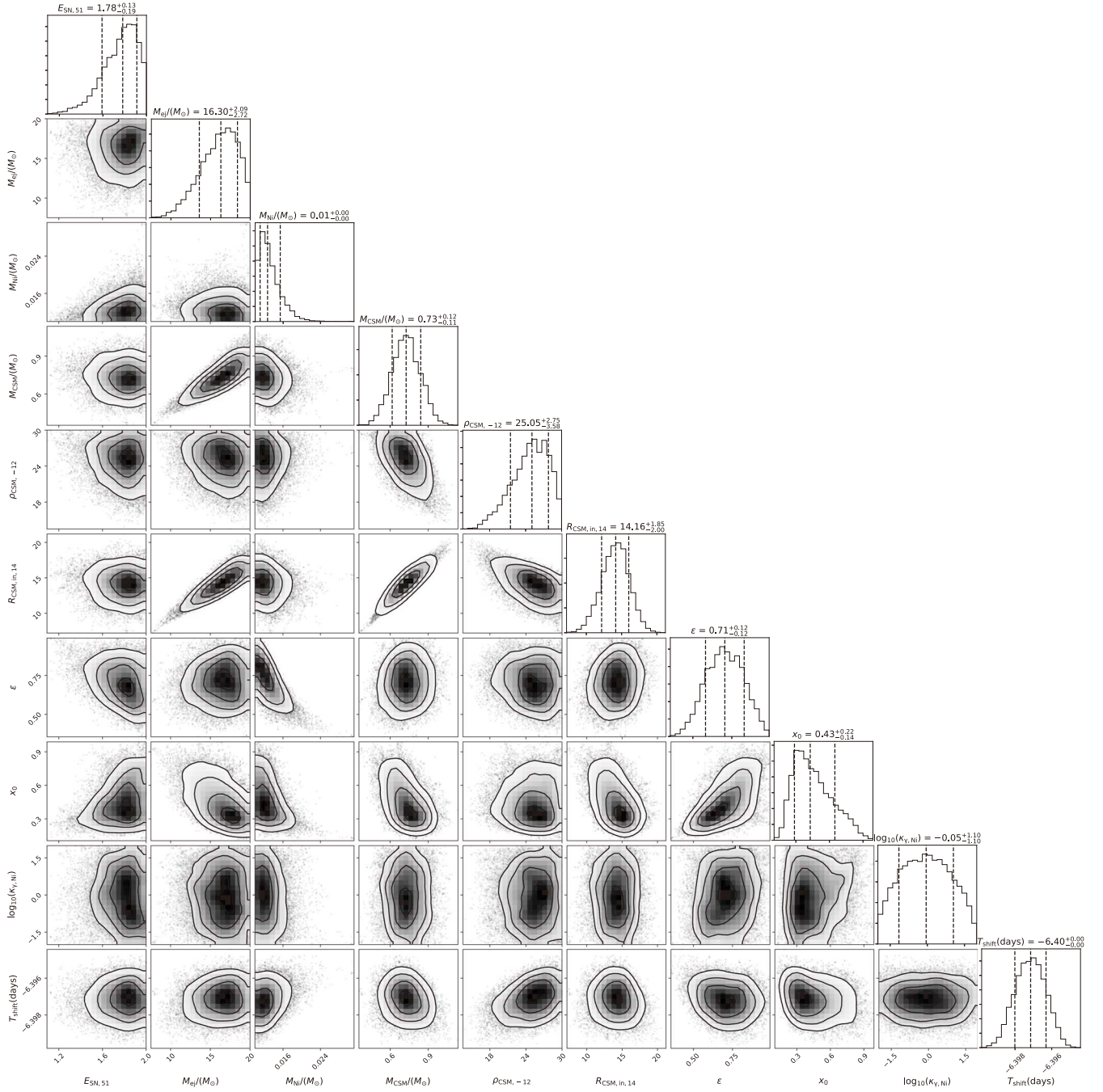


Figure 14. Corner plot of the ^{56}Ni + CSI shell model displaying covariance of estimated parameters.





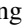




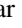
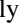

emission features. The estimated line velocities are lower than the average SN Ibn, but they show a faster evolution compared to the group of SNe that show prominent emission features from the beginning.

We are thankful for the support of the staff of the Xinglong 2.16 m and Lijiang 2.4 m telescope, and observing assistants at the 1.04 m ST, 1.30 m DFOT, and 2.00 m HCT for their support during observations. This work was partially supported by the Open Project Program of the Key Laboratory of Optical Astronomy, National Astronomical Observatories, Chinese Academy of Sciences. Funding for the Lijiang 2.4 m telescope has been provided by Chinese Academy of Sciences and the

People's Government of Yunnan Province. We acknowledge Weizmann Interactive Supernova data REpository (WiSeREP; <http://wiserep.weizmann.ac.il>). D.A.H. acknowledges support from NSF grant AST-1313404. The work of X.W. is supported by the National Natural Science Foundation of China (NSFC grants 11325313, 11633002, and 11761141001), and the National Program on Key Research and Development Project (grant No. 2016YFA0400803). This work makes use of data obtained with the LCO Network. K.M. and S.B.P. acknowledges BRICS grant DST/IMRCD/BRICS/Pilotcall/ProFCheap/2017(G) for the present work. S.B.P. and K.M. also acknowledge the DST/JSPS grant, DST/INT/JSPS/P/281/2018. K.M. acknowledges the support from Department

of Science and Technology (DST), Govt. of India and Indo-US Science and Technology Forum (IUSSTF) for the WISTEMM fellowship and Dept. of Physics, UC Davis where a part of this work was carried out. G.C.A., B.K., and D.K.S. acknowledge BRICS grant DST/IMRCD/BRICS/PilotCall1/MuMeSTU/2017(G) for the present work. The work of S.Q.W. is supported by National Natural Science Foundation of China (grants 11963001, 11533003, 11603006, 11673006, 11851304, and U1731239).

ORCID iDs

Anjasha Gangopadhyay  <https://orcid.org/0000-0002-3884-5637>
 Kuntal Misra  <https://orcid.org/0000-0003-1637-267X>
 Shan-Qin Wang  <https://orcid.org/0000-0001-7867-9912>
 Griffin Hosseinzadeh  <https://orcid.org/0000-0002-0832-2974>
 Xiaofeng Wang  <https://orcid.org/0000-0002-7334-2357>
 Stefano Valenti  <https://orcid.org/0000-0001-8818-0795>
 Jujia Zhang  <https://orcid.org/0000-0002-8296-2590>
 D. Andrew Howell  <https://orcid.org/0000-0003-4253-656X>
 Iair Arcavi  <https://orcid.org/0000-0001-7090-4898>
 Brajesh Kumar  <https://orcid.org/0000-0001-7225-2475>
 Curtis McCully  <https://orcid.org/0000-0001-5807-7893>
 Tianmeng Zhang  <https://orcid.org/0000-0002-8531-5161>

References

- Andrews, J. E., & Smith, N. 2018, *MNRAS*, **477**, 74
 Arnett, W. D. 1980, *ApJ*, **237**, 541
 Arnett, W. D. 1982, *ApJ*, **253**, 785
 Becker, A. 2015, HOTPANTS: High Order Transform of PSF ANd Template Subtraction (v 5.1.10b), Astrophysics Source Code Library, ascl:1504.004
 Chatzopoulos, E., Wheeler, J. C., & Vinko, J. 2012, *ApJ*, **746**, 121
 Chevalier, R. A. 1982, *ApJ*, **258**, 790
 Chevalier, R. A., & Fransson, C. 1994, *ApJ*, **420**, 268
 Chugai, N. N., & Danziger, I. J. 1994, *MNRAS*, **268**, 173
 Cooke, J., Ellis, R. S., Nugent, P. E., et al. 2010, *ATel*, **2491**, 1
 Crowther, P., & Smartt, S. 2007, *A&G*, **48**, 1.35
 Fassia, A., Meikle, W. P. S., Chugai, N., et al. 2001, *MNRAS*, **325**, 907
 Foley, R. J., Smith, N., Ganeshalingam, M., et al. 2007, *ApJL*, **657**, L105
 Fremling, C., Dugas, A., & Sharma, Y. 2019, Transient Name Server Classification Report, No. 2019-9
 Gal-Yam, A. 2014, AAS Meeting Abstracts, **223**, 235.02
 Gal-Yam, A., Arcavi, I., Ofek, E. O., et al. 2014, *Natur*, **509**, 471
 Ginzburg, S., & Balberg, S. 2012, *ApJ*, **757**, 178
 Gorbikov, E., Gal-Yam, A., Ofek, E. O., et al. 2014, *MNRAS*, **443**, 671
 Hakobyan, A. A., Adibekyan, V. Z., Aramyan, L. S., et al. 2012, *A&A*, **544**, A81
 Hosseinzadeh, G., Arcavi, I., Valenti, S., et al. 2017, *ApJ*, **836**, 158
 Hosseinzadeh, G., McCully, C., Zabludoff, A. I., et al. 2019, *ApJL*, **871**, L9
 Jordi, K., Grebel, E. K., & Ammon, K. 2006, *A&A*, **460**, 339
 Karamahmetoglu, E., Fransson, C., Sollerman, J., et al. 2019, arXiv:1910.06016
 Khazov, D., Yaron, O., Gal-Yam, A., et al. 2016, *ApJ*, **818**, 3
 Liu, L.-D., Wang, L.-J., Wang, S.-Q., & Dai, Z.-G. 2018, *ApJ*, **856**, 59
 Lusk, J. A., & Baron, E. 2017, *PASP*, **129**, 044202
 Lyman, J. D., Bersier, D., James, P. A., et al. 2016, *MNRAS*, **457**, 328
 Morozova, V., Piro, A. L., & Valenti, S. 2017, *ApJ*, **838**, 28
 Munari, U., & Zwitter, T. 1997, *A&A*, **318**, 269
 Nicholl, M. 2018, *RNAAS*, **2**, 230
 Nyholm, A., Sollerman, J., Taddia, F., et al. 2017, *A&A*, **605**, A6
 Pastorello, A., Benetti, S., Brown, P. J., et al. 2015a, *MNRAS*, **449**, 1921
 Pastorello, A., Hadjiyska, E., Rabinowitz, D., et al. 2015b, *MNRAS*, **449**, 1954
 Pastorello, A., Mattila, S., Zampieri, L., et al. 2008, *MNRAS*, **389**, 113
 Pastorello, A., Prieto, J. L., Elias-Rosa, N., et al. 2015c, *MNRAS*, **453**, 3649
 Pastorello, A., Smartt, S. J., Mattila, S., et al. 2007, *Natur*, **447**, 829
 Pastorello, A., Wang, X. F., Ciabattari, F., et al. 2016, *MNRAS*, **456**, 853
 Pastorello, A., Wyrzykowski, L., Valenti, S., et al. 2015d, *MNRAS*, **449**, 1941
 Poznanski, D., Prochaska, J. X., & Bloom, J. S. 2012, *MNRAS*, **426**, 1465
 Prentice, S. J., Ashall, C., James, P. A., et al. 2019, *MNRAS*, **485**, 1559
 Prentice, S. J., Mazzali, P. A., Pian, E., et al. 2016, *MNRAS*, **458**, 2973
 Sanders, N. E., Soderberg, A. M., Foley, R. J., et al. 2013, *ApJ*, **769**, 39
 Schlafly, E. F., & Finkbeiner, D. P. 2011, *ApJ*, **737**, 103
 Schlegel, E. M. 1990, *MNRAS*, **244**, 269
 Shivvers, I., Zheng, W. K., Mauerhan, J., et al. 2016, *MNRAS*, **461**, 3057
 Silverman, J. M., Kleiser, I. K. W., Morton, A. J. L., & Filippenko, A. V. 2010, *CBET*, **2223**, 1
 Smith, N., Foley, R. J., & Filippenko, A. V. 2008, *ApJ*, **680**, 568
 Stetson, P. B. 1987, *PASP*, **99**, 191
 Sun, N.-C., Maund, J. R., Hirai, R., Crowther, P. A., & Podsiadlowski, P. 2020, *MNRAS*, **491**, 6000
 Taddia, F., Stritzinger, M. D., Sollerman, J., et al. 2013, *A&A*, **555**, A10
 Tody, D. 1986, *Proc. SPIE*, **627**, 733
 Tody, D. 1993, in ASP Conf. Ser. 52, IRAF in the Nineties, ed. R. J. Hanisch, R. J. V. Brissenden, & J. Barnes (San Francisco, CA: ASP), 173
 Valenti, S., Fraser, M., Benetti, S., et al. 2011, *MNRAS*, **416**, 3138
 Valenti, S., Howell, D. A., Stritzinger, M. D., et al. 2016, *MNRAS*, **459**, 3939
 Valenti, S., Sand, D., Pastorello, A., et al. 2014, *MNRAS*, **438**, L101
 Wang, S.-Q., & Li, L. 2019, arXiv:1905.12623
 Zhang, J., Xing, L., & Wang, X. 2019, *ATel*, **12410**, 1